17th World Conference on Earthquake Engineering, 17WCEE
Sendai, Japan - September 13th to 18th 2020

SOURCE, PATH, AND SITE EFFECTS ON STRONG MOTIONS DURING THE 2018 Mw 6.6 HOKKAIDO EASTERN IBURI EARTHQUAKE

Y.P. Dhakal[(1)], W. Suzuki[(2)], T. Kunugi[(3)], T. Kimura[(4)], S. Aoi[(5)]

[(1)] *Research Fellow, National Research Institute for Earth Science and Disaster Resilience, Tsukuba, Japan, ydhakal@bosai.go.jp*
[(2)] *Chief Researcher, National Research Institute for Earth Science and Disaster Resilience, Tsukuba, Japan, wsuzuki@bosai.go.jp*
[(3)] *Chief Researcher, National Research Institute for Earth Science and Disaster Resilience, Tsukuba, Japan, kunugi@bosai.go.jp*
[(4)] *Chief Researcher, National Research Institute for Earth Science and Disaster Resilience, Tsukuba, Japan, tkimura@bosai.go.jp*
[(5)] *Director-General, National Research Institute for Earth Science and Disaster Resilience, Tsukuba, Japan, aoi@bosai.go.jp*

Abstract

Analysis of earthquake source, propagation path, and site effects is important in seismic hazard estimation. Particularly, the velocity pulses due to forward rupture directivity effect and local amplification of seismic waves due to unconsolidated sediments are of major concern in the design of engineering structures. The 2018 Mw 6.6 Hokkaido eastern Iburi earthquake caused loss of lives, resulted in the collapse of residential buildings, induced thousands of landslides, and brought damages to lifelines. In this paper, we present the most prominent features of the strong-motion records obtained during the earthquake and discuss the features in terms of the source, path, and site effect. Based on the strong-motion recordings, available velocity models, aftershock distributions, and inverted fault source models, we found that the combined effect of source and site played a significant role in the generation of large velocity pulses at some sites near the epicentral area of the earthquake. At sites in a sedimentary basin, frequencies lower than about 1 Hz were amplified by an order of magnitude compared to that at the basin edge site. At regional distances over about 100 km, the data revealed the lower attenuation of the higher frequency components in the fore-arc region than that in the back-arc region, in line with the heterogeneous attenuation structure in northeast Japan. On average, we found larger values for the horizontal component ground motions in wide frequency ranges at the ocean bottom sites than at the land sites even though the sites were located in the fore-arc region. In particular, the difference was larger at lower frequencies. Previous studies showed that the regional attenuation structure was not sensitive to the lower frequencies. Therefore, we attribute the difference at the lower frequencies to the difference between the site conditions such as the rock sites versus soil sites and sedimentary basins.

Keywords: The 2018 Mw 6.6 Hokkaido eastern Iburi earthquake, directivity effect, attenuation, nonlinear site amplification, MOWLAS

© The 17th World Conference on Earthquake Engineering

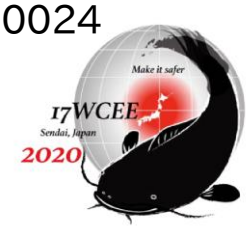

1. Introduction

The 2018 Hokkaido eastern Iburi earthquake occurred on September 6, 03:08 JST (UTC + 9 hours). The epicenter of the earthquake was located on the western foreland area of a collision zone known as Hidaka collision zone (e.g., Kimura 1996) [1] (Figs. 1, 2). The Japan Meteorological Agency (JMA) magnitude (Mj) and focal depth were 6.7 and 37 km, respectively. The moment magnitude (Mw) value determined by USGS (2018) was 6.6. The earthquake caused loss of 42 lives, resulted in a total collapse of 462 and partial collapse of 1,570 residential buildings, and brought significant damage to lifelines (e.g., Cabinet Office Japan 2019; Takahashi and Kimura 2019) [2, 3]. The casualties and damages were primarily related to geotechnical failures such as landslides and liquefaction. Hereafter, the above earthquake is referred to as Iburi earthquake in this paper.

The earthquake was followed by many aftershocks. The earthquake was recorded by many strong-motion accelerometers operated by National Research Institute for Earth Science and Disaster Resilience (NIED) and JMA. Based on the available hypocenter information of aftershocks and focal mechanisms, many researchers constructed fault surface geometry and then performed waveform inversion of long-period components (> 2 s). Researchers proposed fault models with two or three planar fault segments (e.g., Asano and Iwata 2019, Kobayashi et al. 2019) [4, 5] and also fault model with curved surface (Kubo et al. 2020) [6]. In general, the fault geometry had a length of approximately 30 km in the dominant dimension (fault length) and 20 km in the shorter dimension (dip direction). The dip angles were 65-70 degrees dipping towards the east. The minor fault segment in the model by Kobayashi et al. (2019) [5] was dipping towards the west. As the used data and method overlapped largely, the results of waveform inversion were similar. All the models predict large slips at almost the same place and at the same time after the origin of the earthquake, though the models are different in details of slip distribution and fault geometry.

The maximum horizontal vector PGA of 1429 cm/s^2 was observed at the KiK-net site IBUH01 (Oiwake) during the Iburi earthquake. The horizontal vector PGV at the site was 126 cm/s. The JMA instrumental intensity of 6.7 was calculated at the site IBUH01. This value of 6.7 corresponds to the upper limit of JMA intensity on a discrete scale of 0 to 7 (JMA 2018) [7]. The maximum horizontal vector PGV was approximately 151 cm/s, which was recorded at two sites: K-NET site HKD126 (Mukawa) and KiK-net site IBUH03 (Atsuma). The JMA instrumental intensity of 6.4 and 6.2 was calculated at the HKD126 and IBUH03, respectively; these values correspond to the intensity of 6 Upper in the JMA intensity scale. The JMA Atsuma station (47004) recorded horizontal vector PGV of ~132 cm/s, and the JMA instrumental intensity was approximately 6.5. For a quick comparison, the horizontal vector PGVs of ~162 cm/s was recorded at the JR Takatori station during the Mw 6.9, 1995 Kobe earthquake, and ~183 cm/s at Mashiki Town Hall during the Mw 7.1, 2016 Kumamoto earthquake. The ground motions from both earthquakes caused significant damages to buildings and infrastructures and loss of human lives (e.g., Kawase 1996, Kawase et al. 2017) [8, 9]. The spatial distributions of horizontal vector PGAs and PGVs for the Iburi earthquake are displayed in Fig. 1.

In this paper, we describe the most prominent features of recorded ground motions at selected sites during the Iburi earthquake: the source and site amplification effects at small distances, basin effects on long-period components, and regional path effects on the short period components of recorded ground motions during the earthquake. We investigated in some detail the nonlinear site amplification at smaller distances in our previous study (Dhakal et al. 2019) [10] and made it shorter in the present study. We used strong-motion data from K-NET [11], KiK-net [11], and S-net [12] of NIED, and also from JMA.

© The 17th World Conference on Earthquake Engineering

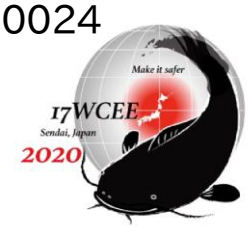

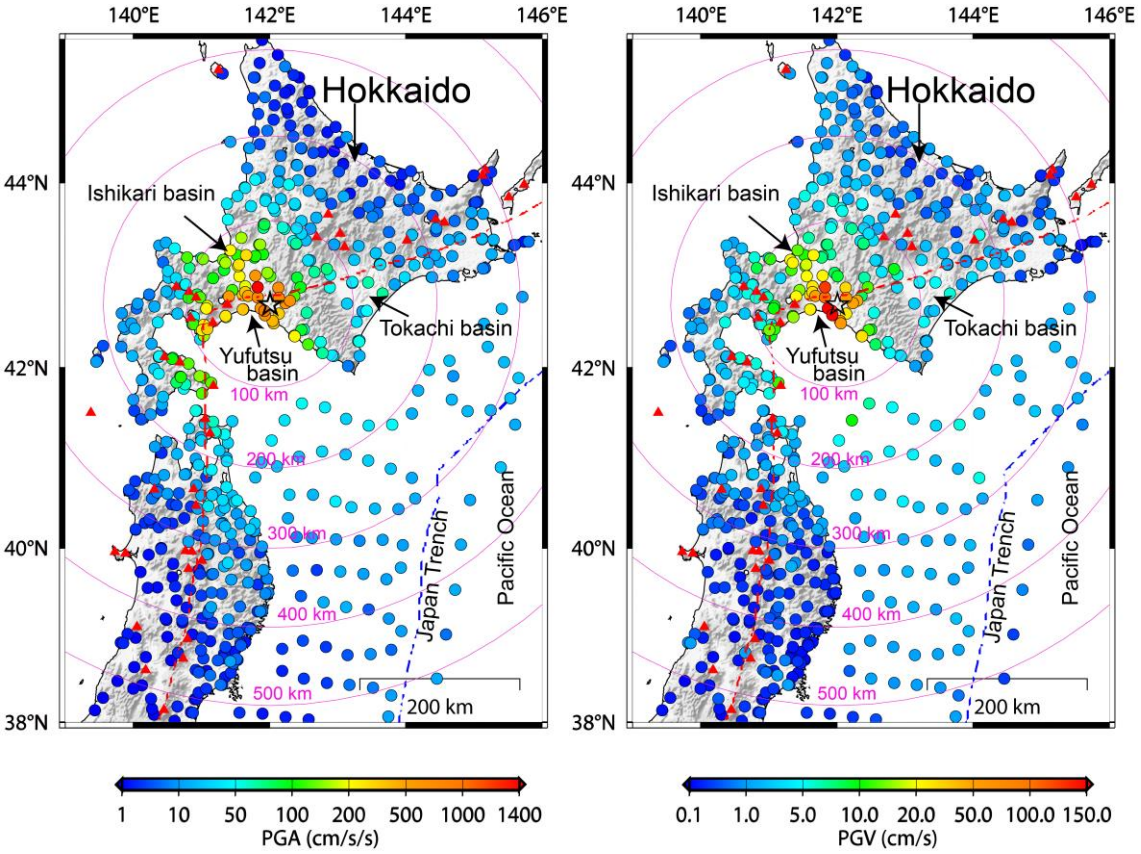

Fig. 1 – Spatial distribution of horizontal vector PGAs (left panel) and PGVs (right panel). The star denotes the epicenter of the 2018, Mw 6.6 Hokkaido eastern Iburi earthquake. The red triangles denote the active volcanoes, and the red dashed line denotes the volcanic front.

2. Source Effect

We present here velocity waveforms obtained by the integration of accelerograms at sites around the epicenter. Fig. 2 shows the location of the sites and Fig. 3 shows the north-south (NS) and east-west (EW) component velocity waveforms in the left and right panels, respectively. The waveforms in Fig. 3 are arranged in the clockwise order of the sites beginning from the HKD126 site located south of the epicenter. The EW components at HKD126, 47004, and IBUH03 show the large velocity pulses. The PGV values of the EW components are about three times the values of the NS components at the HKD126 and IBUH3 sites. The dominance of one component over another component cannot be seen on the waveforms at the HKD128 sites even though the PGVs on both components are about 100 cm/s. The epicenter locations of the aftershocks that occurred within 12 hours after the mainshock are shown by blue circles. Based on the focal mechanism plot based on F-net [13], NIED, together with the aftershocks and previous studies, the fault was a reverse fault dipping towards east. All the sites located east of the epicenter of the mainshock had relatively small PGVs. It can be also seen in Fig. 3 that the sites in the east of the epicenter are generally rich in high frequency components. The difference on the frequency components generally reflect the difference of site amplifications. In fact, the sites with large PGVs of ~ 100 cm/s are located on relatively thick sediments of the Yufutsu plain while the sites in the east are located on shallow sediment covers over the basement rocks. It has been known that the fault-normal components generally have pulse-like waveforms and larger PGVs due to the shear-rupture propagation effect (e.g., Sommerville et al. 1997) [14] than the fault-parallel components at sites located in the direction of rupture propagation. The NS and EW components roughly

© The 17th World Conference on Earthquake Engineering

match with the fault-parallel and fault-normal directions for this earthquake. As the focal depth was 37 km and the sites HKD126, 47004, and IBUH03 were located in the rupture propagation direction, the large velocity pulses on EW component may be related to the effcet of forward rupture propagation in addition to the large slips near the sites (e.g., Kobyashi et al. 2019) [5], and site amplification effect (e.g., Nakano and Kawase 2019, Takai et al. 2019) [15, 16]. The relatively smaller amplitudes and lack of dominant pulses on any cmponent at east sites (located opposite to the rupture propagation direction) may support for some degree of forward rupture propagation effcet at sites with high PGVs mentioned above.

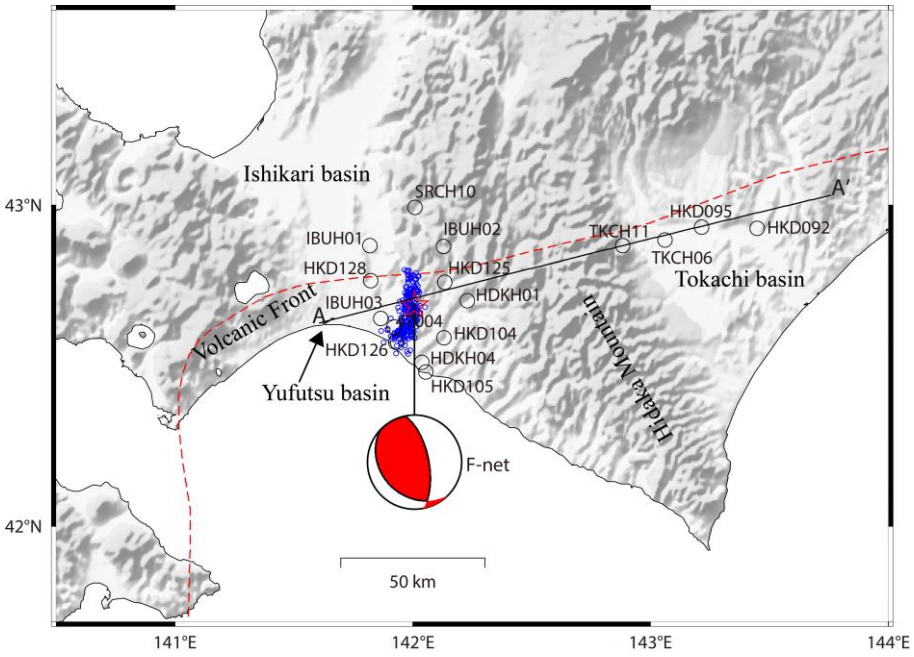

Fig. 2 – Location of strong-motion observation sites (circles). The red star denotes the epicenter of the mainshock, and the blue circles denote the epicenters of the aftershocks within twelve-hours after the occurrence of the mainshock. The black solid line denotes the surface profile line of the vertical cross section of the velocity model depicted in Fig. 5. The focal mechanism plot is from F-net, NIED.

3. Site Amplification Effect

We examined nonlinear site responses during the Iburi earthquake at 16 KiK-net sites based on surface-to-borehole (S-to-B) spectral ratios of S-waves and at another 16 K-NET sites based on horizontal-to-vertical spectral ratios of S-waves, and presented the results in our earlier paper (Dhakal et al. 2019) [10]. Also, the nonlinear site response classification was carried out at a large number of sites in Ji et al. (2019) [17]. Here, we only show and discuss the comparison of the S-to-B spectral ratios of S-waves at four KiK-net sites, namely IBUH01, IBUH02, HDKH01, IBUH03, where the nonlinear effects were conspicuous. The spectral ratios are plotted in Fig. 4 in which the sites are arranged in the order of decreasing horizontal vector PGA during the Iburi earthquake from left to right panels, a to d, respectively. The S-to-B spectral ratios for weak motions may be considered to be linear site amplifications by the sediments between the borehole and surface. The spectral ratios for the mainshock at the sites corroborated the two most well-known features of nonlinearity: the reduction of high-frequency components and shift of predominant frequency towards lower one in comparison to those for the weak motions. We expressed the change in peak frequencies during the mainshock in comparison to the weak-motions as (Fw-Fs) *100/Fw, where Fw and Fs are the peak frequencies of weak-motion, and strong-motion spectral ratios. The percentage changes in predominant frequencies of the sites were approximately 80% at IBUH01 (Fig. 4a), 38% at IBUH02 (Fig. 4b), 62% at HDKH01 (Fig. 4c), and 73% at IBUH03 (Fig. 4d). Nonlinear site amplification effect was also suspected for

© The 17th World Conference on Earthquake Engineering

vertical component recordings at some sites based on borehole spectral ratios of S-wave portions on vertical components. We refer our previous paper (Dhakal et al. 2019) [10] to interested readers.

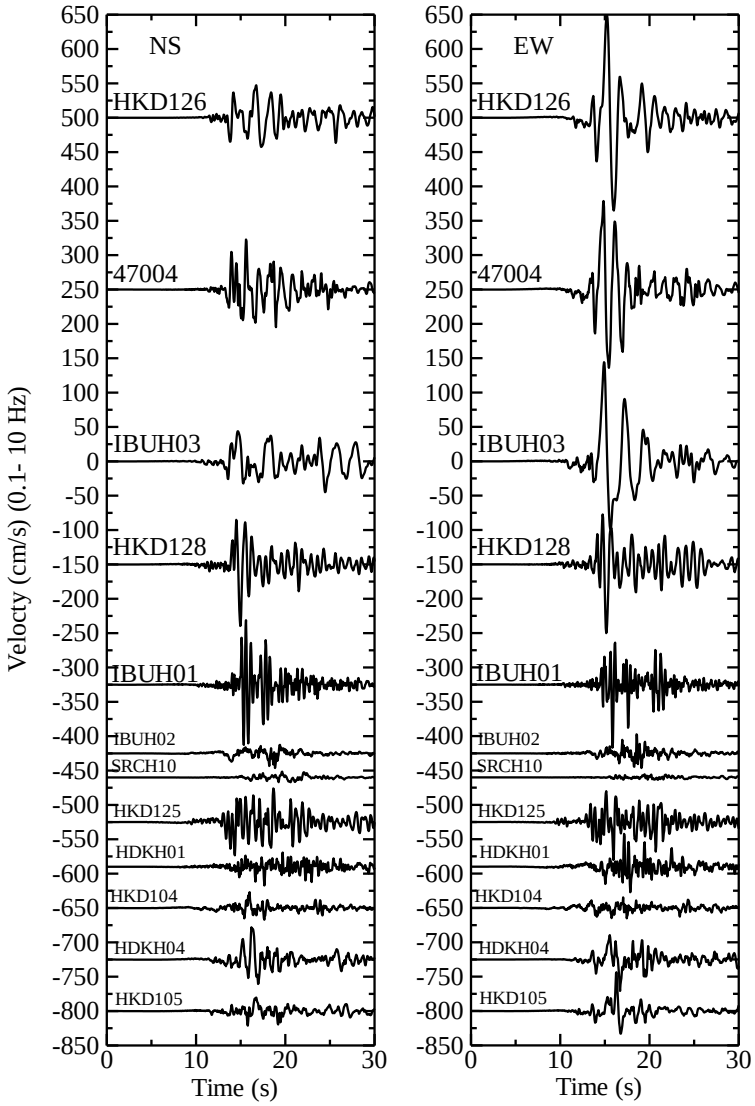

Fig. 3 – Velocity seismograms at sites around the epicenter obtained by integration of accelerograms. See Fig. 2 for location of the sites. Site codes are provided near the corresponding traces. The records were bandpass filtered between 0.1 and 10 Hz. NS and EW denote the north-south and east-west components, respectively.

© The 17th World Conference on Earthquake Engineering

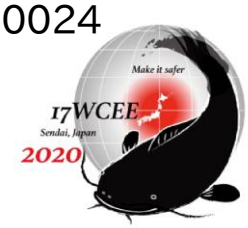

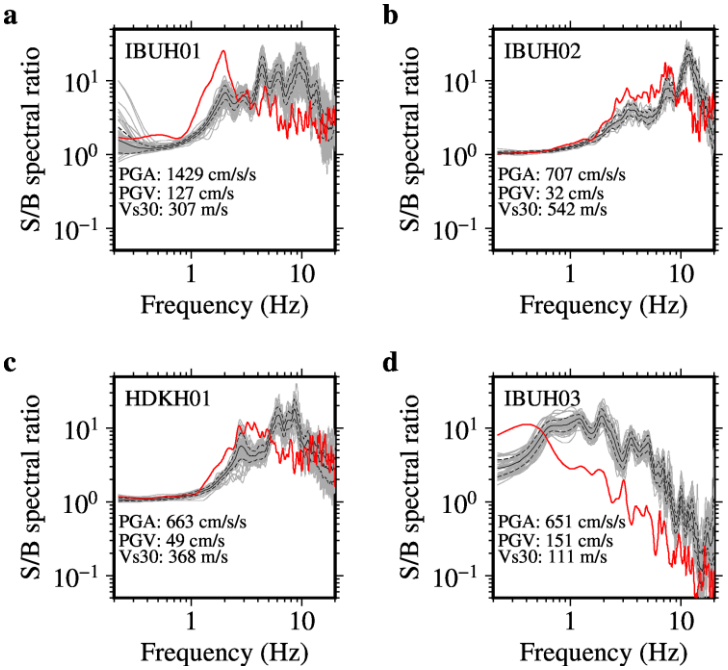

Fig. 4 – Surface-to-borehole (S/B) S-wave spectral ratios of horizontal component recordings during weak-motions (grey lines) and those during the mainshock (red lines). Solid black lines denote mean spectral ratios for weak motions and dashed grey lines denote one standard deviation. The plots in order of decreasing horizontal vector PGAs in panels a to d, respectively. The site codes are indicated in each panel. See Fig. 2 for site locations.

4. Basin Amplification Effect

Because of the growing number of tall buildings located on sedimentary basins, it is essential to evaluate the basin amplification effect at sites located on the sedimentary basins. In this paper, we show a comparison of the waveforms at the TKCH011 site located on the western edge of the Tokachi basin and three other sites, namely, TKCH06, HKD095, and HKD092, located on the basin (see Fig. 2 for the site locations). The western edge of the Tokachi basin is located about 70 km away from the epicenter. A surface profile line, A-A', connecting the epicenter and Tokachi basin, is shown in Fig. 2. The vertical section of JIVSM (Japan Integrated Velocity Structure Model, Koketsu et al. 2012) [18] along the profile A-A' is shown in Fig. 5. The approximate location of the sites under consideration is depicted on the profile. The velocity model indicates that the seismic waves are considered to reach the basin edge site first and then the basin sites. Figure 6a shows a comparison of the NS component accelerograms at the TKCH11 and HKD095 sites. The waveforms were aligned with respect to the theoretical S-wave arrivals from the hypocenter. The Fourier spectral amplitudes for three different time-windows, which are indicated in Fig. 6a, are plotted in Fig. 6b. It can be seen that the spectral amplitudes at frequencies of about 3 Hz are larger at the S-wave window part (first time-window) at the basin edge-site than those at the basin site. At frequencies lower than about 2 Hz, the spectral amplitudes at the basin sites are larger, and the difference becomes remarkable for the second and third time-windows. The ratios of spectral amplitudes at frequencies lower than about 1 Hz are about 10 for the later phases while the ratios are about 2 to 3 for the time window containing the S-waves. It is interesting to note that the PGA at the TKCH11 site is larger than the PGA at the HKD095 site. The velocity seismograms at the four sites that roughly aligned along a straight line depicted in Fig. 2 are plotted in Fig. 6c. It can be seen that the PGV at the basin edge site is from the S-wave part while the PGVs at the TKCH06 and HKD095 are from the later part of the corresponding waveforms. The velocity waveforms have larger

© The 17th World Conference on Earthquake Engineering

amplitudes and continue for longer durations at the basin sites while the amplitudes decrease sharply at the basin edge site. The observed velocity waveforms are generally in line with the basin structure model. A thicker low-velocity layer exists beneath the TKCH06 and HKD095 sites than at the HKD092 site. The larger amplitude for the later phases at the TKCH06 and HKD095 sites and relatively lower amplitudes of the later phases at the HKD092 site may be attributed to the variation of the thickness of the low-velocity layer beneath the sites. Considering the source duration of about 10 s, the elongation of the duration at the basin sites may be attributed to the entrapment of seismic waves by the basin sediments. It is, therefore, important to validate and improve the velocity models based on a comparison between the observed and synthetic waveforms for the evaluation of seismic hazards from future earthquakes.

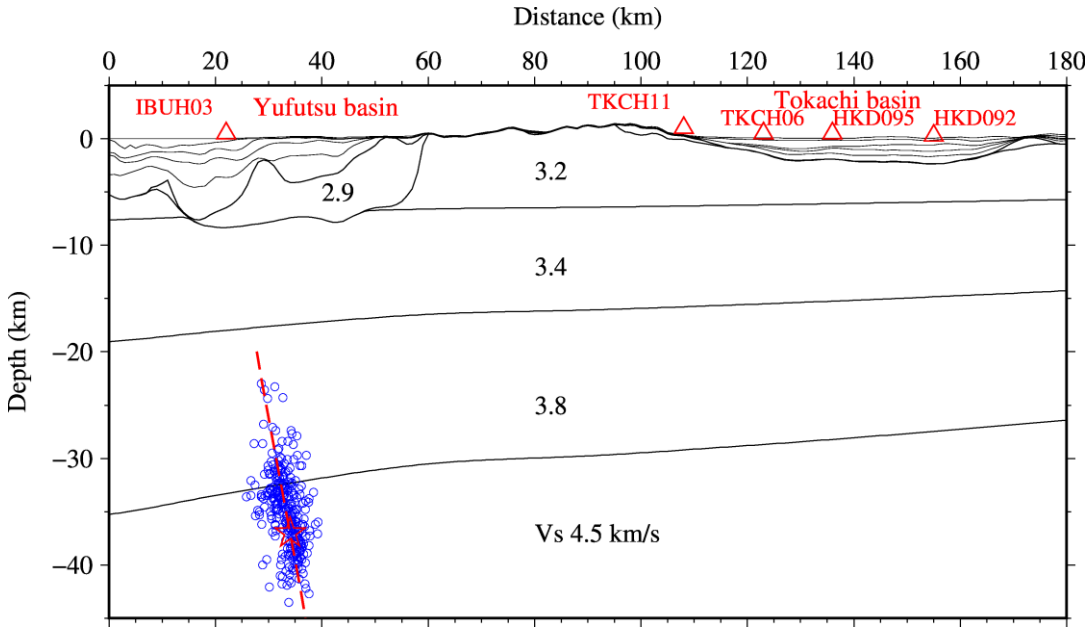

Fig. 5 – Vertical cross-section of Japan Integrated Velocity Model (JIVSM; Koketsu et al. 2012) [13] along the surface profile (A-A') shown in Fig. 2. See the text for further explanation.

5. Path Effects

In our previous paper (Dhakal et al. 2019) [10], we showed that the PGAs on the fore-arc side of the volcanic front were larger than those on the back-arc side at distances over about 100 km for the Iburi earthquake. On the other hand, the difference was small for PGVs. These results were generally desirable because the relatively long period ground motions, of which the PGV may be a good representative, become less sensitive to very shallow earth structures compared to the short-period ground motions. Dhakal et al. (2010) [19] reported that the distinction of fore-arc and back-arc data becomes less obvious at periods larger than about 0.5 s. Here we show the plots of pseudo-velocity response spectra at periods of 0.1, 0.3, 0.5, 0.8, 1.0, and 3.0 as a function of hypocentral distances in Fig. 7. The data are color-coded by the values of ratios between the portion of the hypocentral distance in the back-arc side and the hypocentral distance. If R_2 denotes the distance in the back-arc and R1 denotes the distance in the fore-arc, then ratio = $R_2/(R_1+R_2)$. If the ratio (r) = 0, the site belongs to the fore-arc side, otherwise the back-arc side. Figure 7 also shows the values plotted for the S-net data. All the S-net data belong to the group of fore-arc data. In the plots, it can be seen that the data for the fore-arc side have relatively larger values than those for the back-arc side at periods of 0.1, 0.3, and 0.5 s at distances beyond about 100-150 km. The difference at shorter periods may be explained in terms of difference in the Q-structure in the fore-arc and back-arc regions. In the figure, it can be generally seen that the values of the S-net data are similar to those on the fore-arc side land stations at periods lower than about 0.5 s at distances smaller than about 200 km. On the other hand, at the period of 1

© The 17th World Conference on Earthquake Engineering

and 3s, the values of the S-net data are generally larger than those on the fore-arc side land stations at distances over about 200 km. The differences between the land and S-net stations at the longer periods may be attributed to the difference of local subsurface geology beneath the land and ocean bottom stations and the effect of oceanic water at the ocean bottom stations.

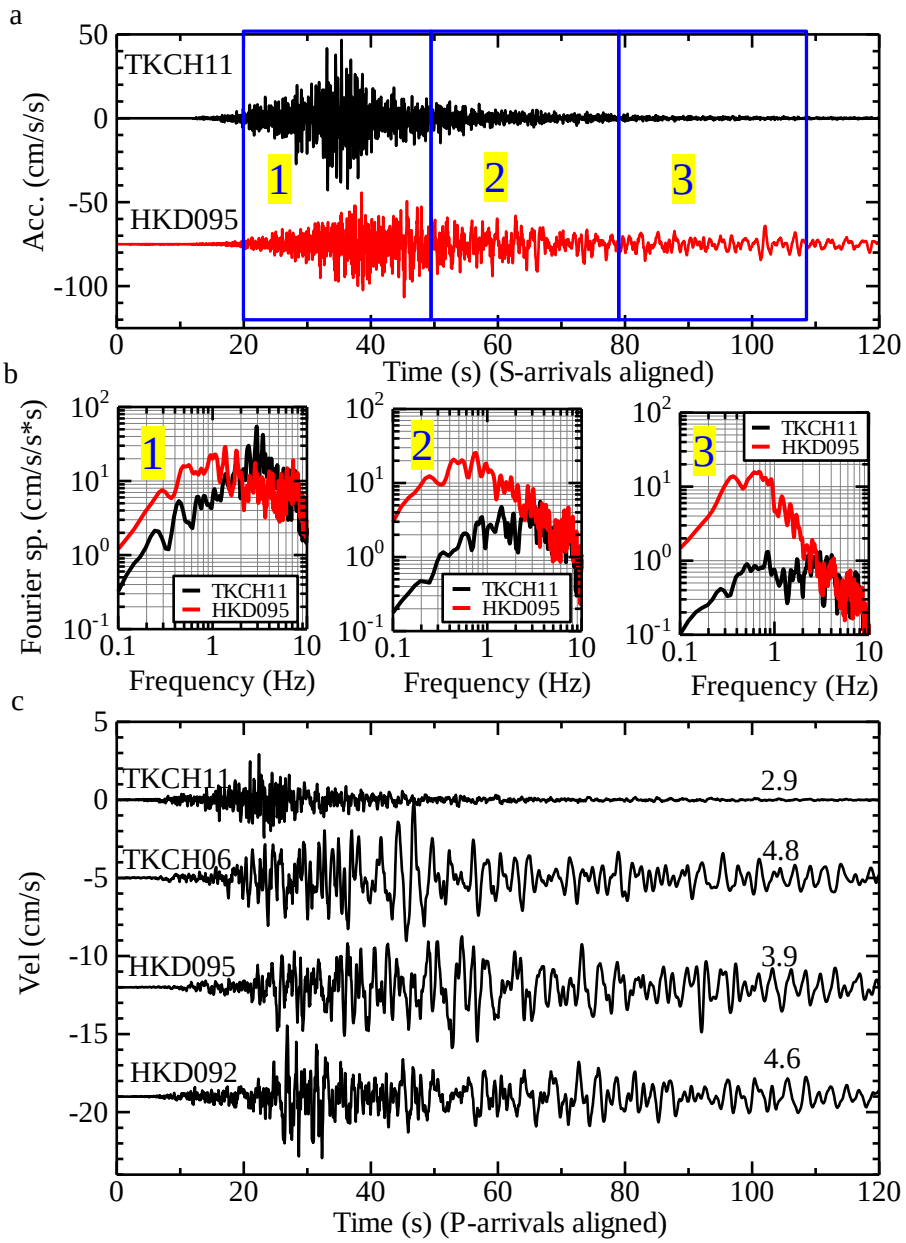

Fig. 6 – a. Comparison of accelerograms at TKCH11 and HKD095; b. Comparison of acceleration Fourier spectral amplitudes at the two sites for three time-windows indicated in a; c. Comparison of velocity seismograms at the basin edge site, TKCH11, and basin sites TKCH06, HKD095, and HKD092, as indicated in the plots. The waveforms were bandpass-filtered between 0.1 and 10 Hz. See Fig. 2 for site locations.

Dhakal et al. (2010) [19] derived separate anelastic attenuation coefficients for the fore-arc and back-arc regions using the interplate and intraslab earthquake data. For reference, the attenuation curves for four values of distance ratios (r = 0.0, 0.3, 0.5, and 0.7) are plotted in each panel in Fig. 7 for the case of an interplate earthquake. The attenuation curves for different ratios generally follow the data distribution of

© The 17th World Conference on Earthquake Engineering

corresponding distance ratios for periods up to around 1 s; the data as well as the attenuation curves become less distinguishable in terms of the distance ratios at the period of 3 s.

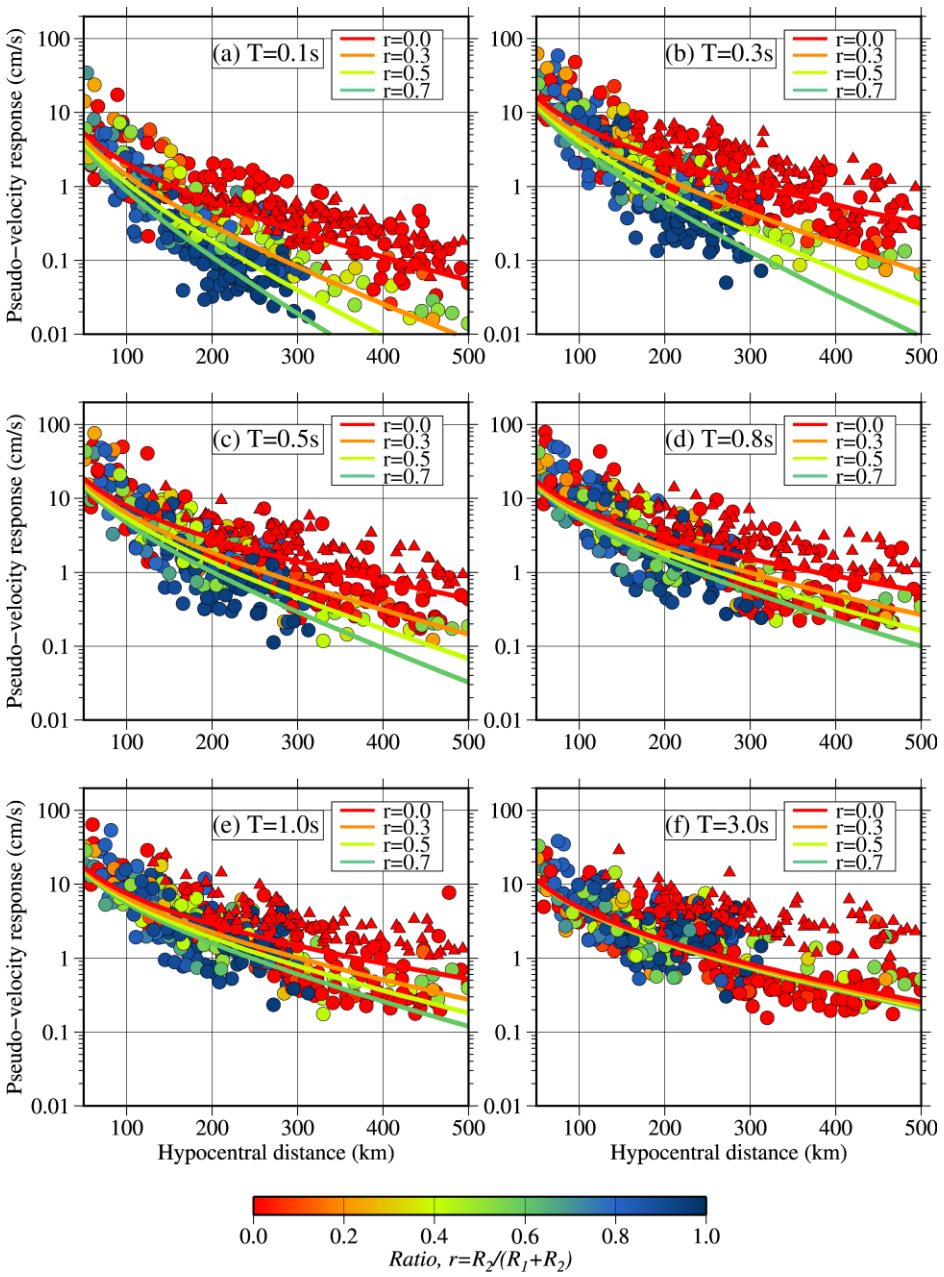

Fig. 7 – Comparison between the observed values and empirical attenuation relationships of maximum pseudo-velocity response values: (a) T = 0.1 s; (b) T = 0.3 s; (c) T =1.0 s; and (d) T = 3.0 s. The observed response values are shown by circles (land stations) and triangles (ocean bottom stations) color-coded by the values of distance ratios of the observation sites. R_1 and R_2 denote the distances from the epicenter to the volcanic front and from the volcanic front to the site, respectively. R_2 = 0 for a site located on the fore-arc region (Pacific Ocean side of the volcanic front). See the text for further explanation.

© The 17th World Conference on Earthquake Engineering

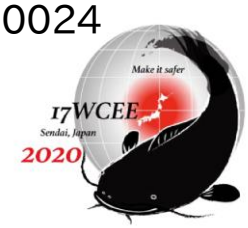

6. Discussions and Conclusions

We analyzed the strong-motion recordings around the epicenter of the 2018 Mw 6.6 Hokkaido eastern Iburi earthquake to understand the source and site effects at small distances. At some sites in the rupture propagation directions, large velocity pulses were observed on the fault-normal components. Such large pulses were not observed at sites opposite to the rupture propagation direction. Also, the recordings with large pulses were richer in lower frequencies than those at the sites in the down-dip direction, and the available recordings showed larger PGVs on the sites west of the epicenter area. Source inversions for the earthquake revealed large slip areas up-dip of the hypocenter. Surface-to-borehole and H/V spectral ratios of S-waves indicated that strong nonlinear site response occurred at many sites causing large frequency shifts to lower frequencies. The available velocity model suggested that the west side of the epicenter area is covered with thick sediments while the sites in the east close to the epicenter area located on not so thick sediments. All the above observations and available data indicate that the source effect, as well as the site effect, were responsible for the large velocity pulses near the epicentral area. Also, the recordings from the earthquake revealed the elongation of duration and amplification of long-period components of ground motions at the sedimentary basin sites. The sites near the center of the Tokachi basin recorded the PGVs from the later phases after the S-waves. The attenuation relationship of the pseudo-velocity response spectra revealed that the attenuation rate of short-period (< about 0.5 s) components of ground motions in the fore-arc is smaller than that in the back-arc side at distances larger than about 100 km. The attenuation relationship also revealed that the ocean bottom motions, on average, had larger amplitudes than those on the land sites at distances beyond about 200 km for the wide period ranges. Previous studies have found high Qs values in the Pacific plate, and the available subsurface model shows the substantial thickness of sediments in the Japan Trench area. Thus, we conclude that the observations indicate a combination of source (large slips and forward rupture propagation) and site (amplification by soft sediments and frequency shift by nonlinear soil response) effects for the large velocity pulses in the near epicenter area; basin amplification effect for the elongation of duration and stronger later phases of long-period components; smaller rate of attenuation on the fore-arc side at shorter periods due to high Qs, and the amplification of long-period components by the oceanic sediments at the ocean bottom stations.

7. Acknowledgments

We used the information on the location and magnitude of earthquakes provided by Japan Meteorological Agency (JMA). We also used a few strong-motion recordings provided by JMA. We used the Generic Mapping Tools (Wessel and Smith 1998 [20]) for drawing some of the figures. We would like to thank an anonymous reviewer for the thoughtful suggestion on the abstract.

8. References

[1] Kimura G (1996): Collision orogeny at arc-arc junctions in the Japanese Islands. The Island Arc **5,** 262-275.

[2] Cabinet Office Japan (2019): About damage situation on the 2018 Hokkaido Eastern Iburi Earthquake, 28 January 2019, 15:00. *http://www.bousai.go.jp/updates/h30jishin_hokkaido/pdf/310128_jishin_hokkaido.pdf*. Accessed 4 March 2019 (In Japanese)

[3] Takahashi H, Kimura R (2019) The 2018 Hokkaido eastern Iburi earthquake and its aftermath. Disaster Report: Sc20190112. *Journal of Disaster Research*, **14**, Scientific Communication

[4] Asano K, Iwata T (2019) Source rupture process of the 2018 Hokkaido Eastern Iburi earthquake deduced from strong-motion data considering seismic wave propagation in three-dimensional velocity structure. *Earth, Planets and Space*, **71**, 101

[5] Kobayashi H, Koketsu K, Miyake H (2019): Rupture process of the 2018 Hokkaido Eastern Iburi earthquake derived from strong motion and geodetic data. *Earth, Planets and Space*, **71**, 63

© The 17th World Conference on Earthquake Engineering

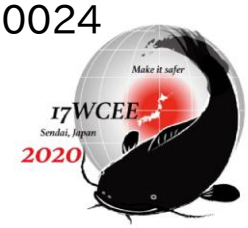

[6] Kubo H, Iwaki A, Suzuki W, Aoi S, Sekiguchi H (2020): Estimation of the source process and forward simulation of long-period ground motion of the 2018 Hokkaido Eastern Iburi, Japan, earthquake. *Earth, Planets and Space. https://doi.org/10.1186/s40623-020-1146-z*

[7] JMA (Japan Meteorological Agency) (2018): *https://www.jma.go.jp/jma/en/Activities/inttable.pdf*. Accessed 27 November 2018

[8] Kawase H (1996): The cause of the damage belt in Kobe: the basin-edge effect, constructive interference of the direct S-wave with the basin-induced diffracted/Rayleigh waves. *Seismol Res Lett* **67**(5), 25-34

[9] Kawase H, Matsushima S, Nagashima F, Baoyintu, Nakano K (2017): The cause of heavy damage concentration in downtown Mashiki inferred from observed data and field survey of the 2016 Kumamoto earthquake. *Earth, Planets and Space* **69**, 3

[10] Dhakal YP, Kunugi T, Kimura T, Wataru S, Aoi S (2019): Peak ground motions and characteristics of nonlinear site response during the 2018 Mw 6.6 Hokkaido eastern Iburi earthquake. *Earth, Planets and Space*, **71**, 56.

[11] National Research Institute for Earth Science and Disaster Resilience (2019): NIED K-NET, KiK-net, *National Research Institute for Earth Science and Disaster Resilience*, doi:10.17598/NIED.0004

[12] National Research Institute for Earth Science and Disaster Resilience (2019): NIED S-net, *National Research Institute for Earth Science and Disaster Resilience*, doi:10.17598/NIED.0007

[13] National Research Institute for Earth Science and Disaster Resilience (2019): NIED F-net, *National Research Institute for Earth Science and Disaster Resilience*, doi:10.17598/NIED.0005

[14] Sommerville PG, Smith NF, Graves RW, Abrahamson NA (1997): Modification of empirical attenuation relations to include the amplitude and duration effects of rupture directivity. *Seismol Res Lett* **70**, 59–80

[15] Nakano K, Kawase H (2019): Source parameters and site amplifications estimated by generalized inversion technique: focusing on the 2018 Hokkaido Iburi-Tobu earthquake. *Earth, Planets and Space*, **71,** 66

[16] Takai N, Shigefuji M, Horita J, Nomoto S, Maeda T, Ichiyanagi M, Takahashi H, Yamanaka H, Chimoto K, Tsuno S, Korenaga M, Yamada N (2019): Cause of destructive strong ground motion within 1–2 s in Mukawa town during the 2018 MW 6.6 Hokkaido eastern Iburi earthquake. *Earth Planets Space* **71**, 67

[17] Ji K, Wen R, Ren Y, Dhakal YP (2019): Nonlinear seismic site response classification using K-means clustering algorithm: Case study of the September 6, 2018 Mw6.6 Hokkaido Iburi-Tobu earthquake, Japan. *Soil Dynamics and Earthquake Engineering*, **128**. https://doi.org/10.1016/j.soildyn.2019.105907

[18] Koketsu K, Miyake H, Suzuki H (2012): Japan integrated velocity structure model version 1. *Proceedings of 15th World Conf on Earthq Engg*, Lisbon, Portugal, Paper ID **1773**

[19] Dhakal YP, N Takai, T Sasatani (2010): Empirical analysis of path effects on prediction equations of pseudo-velocity response spectra in northern Japan. *Earthquake Engineering & Structural Dynamics*, **39**, 443–461

[20] Wessel P, Smith WHF (1998): New, improved version of generic mapping tools released. *Eos trans* AGU **79**, 579

© The 17th World Conference on Earthquake Engineering